



Published in final edited form as:

*Med Image Comput Comput Assist Interv.* 2020 October ; 12267: 280–290.

doi:10.1007/978-3-030-59728-3\_28.

## Estimating Tissue Microstructure with Undersampled Diffusion Data via Graph Convolutional Neural Networks

Geng Chen<sup>1</sup>, Yoonmi Hong<sup>1</sup>, Yongqin Zhang<sup>2</sup>, Jaeil Kim<sup>3</sup>, Khoi Minh Huynh<sup>1</sup>, Jiquan Ma<sup>4</sup>, Weili Lin<sup>1</sup>, Dinggang Shen<sup>1</sup>, Pew-Thian Yap<sup>1</sup>, UNC/UMN Baby Connectome Project Consortium

<sup>1</sup>Department of Radiology and BRIC, University of North Carolina, Chapel Hill, USA

<sup>2</sup>School of Information Science and Technology, Northwest University, Xi'an, China

<sup>3</sup>School of Computer Science and Engineering, Kyungpook National University, Daegu, South Korea

<sup>4</sup>Department of Computer Science and Technology, Heilongjiang University, Harbin, China

### Abstract

Advanced diffusion models for tissue microstructure are widely employed to study brain disorders. However, these models usually require diffusion MRI (DMRI) data with densely sampled  $q$ -space, which is prohibitive in clinical settings. This problem can be resolved by using deep learning techniques, which learn the mapping between sparsely sampled  $q$ -space data and the high-quality diffusion microstructural indices estimated from densely sampled data. However, most existing methods simply view the input DMRI data as a vector without considering data structure in the  $q$ -space. In this paper, we propose to overcome this limitation by representing DMRI data using graphs and utilizing graph convolutional neural networks to estimate tissue microstructure. Our method makes full use of the  $q$ -space angular neighboring information to improve estimation accuracy. Experimental results based on data from the Baby Connectome Project demonstrate that our method outperforms state-of-the-art methods both qualitatively and quantitatively.

### Keywords

Diffusion MRI; Graph CNN; Microstructure imaging

## 1 Introduction

Diffusion MRI (DMRI) is capable of measuring the signal attenuation caused by the anisotropic motion of water molecules in the human nervous system [1-3]. This makes DMRI a unique non-invasive imaging technique for in vivo examination of brain tissue microstructure and white matter pathways. With advanced diffusion models [4-8], DMRI affords rich characterizations of the brain, providing biomarkers useful for diagnosis of brain disorders. However, many microstructure models, e.g., diffusion kurtosis imaging (DKI) [4]

and neurite orientation dispersion and density imaging (NODDI) [5], require DMRI data densely sampled in  $q$ -space, i.e., multi-shell data with a sufficient angular resolution. The  $q$ -space sampling density is determined by the number of acquired diffusion-weighted images (DWIs). Increasing the number of DWIs will inevitably prolong the acquisition time, which can be prohibitive in real-world applications.

Deep learning (DL) techniques have been employed to improve microstructural estimation without requiring dense  $q$ -space sampling [9-15]. A typical example is q-DL [9], which utilizes a multilayer perceptron to learn the relationship between sparsely sampled  $q$ -space data and high-quality microstructure indices estimated from densely sampled  $q$ -space data, thus reducing the acquisition time. Moreover, time-consuming model fitting is replaced by an efficient network. However, this method simply views the DMRI signals in a voxel as a vector without considering  $q$ -space data structure. Signal correlation between angular neighbors is overlooked in the process of microstructural estimation.

To overcome this limitation, we represent DMRI data using graphs and then utilize graph convolutional neural networks (GCNNs) to estimate tissue microstructure. Specifically, we first represent  $q$ -space signal measurements using a graph that encodes the geometric structure of  $q$ -space sampling points. We then utilize residual GCNNs to learn the mapping between sparsely sampled  $q$ -space data and high-quality estimates of microstructure indices. Our method is capable of not only reducing the data acquisition time but also accelerating the estimation procedure. Thanks to the graph representation, our method explicitly takes into account the  $q$ -space data structure and harnesses information from angular neighbors to improve the estimation accuracy of tissue microstructure. We evaluate our method using data from the Baby Connectome Project [16,17]. The results indicate that our method yields microstructural estimates with remarkably improved accuracy.

## 2 Methods

In this section, we will first show how to represent DMRI data using graphs. We will then introduce graph Fourier analysis and its application to fast and localized spectral filtering [18], which is the basis of GCNNs and has been applied in a number of DMRI data prediction tasks [19-22]. Finally, we will describe our network architecture in detail.

### 2.1 Graph Representation of DMRI Data

A graph can be denoted as  $\mathcal{G} = \{\mathcal{V}, \mathcal{E}, W\}$ , where  $\mathcal{V} = \{v_i \in \mathcal{M} : i = 1, \dots, N\}$  is a set of points on a manifold  $\mathcal{M}$ ,  $\mathcal{E} \subset \mathcal{V} \times \mathcal{V}$  is a set of edges connecting the vertices, and  $W = (w_{i,j}) \in \mathbb{R}^{N \times N}$  is an adjacency matrix, which is symmetric with weight  $w_{i,j} > 0$  when nodes  $i$  and  $j$  are connected.

Figure 1 illustrates the graph representation of  $q$ -space. Similar to [23-25], to represent DMRI data using graphs, we define the adjacency weight between two nodes (i.e., sampling points)  $i$  and  $j$  in  $q$ -space using two Gaussian kernels, accounting for differences in gradient directions and diffusion weightings, i.e.,

$$w_{i,j} = \exp\left\{-\frac{1 - (\hat{\mathbf{q}}_i^\top \hat{\mathbf{q}}_j)^2}{2\sigma_a^2}\right\} \exp\left\{-\frac{(\sqrt{b_i} - \sqrt{b_j})^2}{2\sigma_b^2}\right\}, \quad (1)$$

where  $\hat{\mathbf{q}}_i = \mathbf{q}_i / \|\mathbf{q}_i\|$  is a normalized wavevector with  $\mathbf{q}_i \in \mathbb{R}^3$ ,  $b_i = t\mathbf{q}_i^2$  is the corresponding  $b$ -value with diffusion time  $t$ ,  $\sigma_a$  and  $\sigma_b$  are two parameters controlling the bandwidths of two Gaussian kernels. Our formulation of the adjacency weight encourages a large weight to be assigned to two nodes sharing similar gradient directions and diffusion weightings. In this way, the  $q$ -space is represented as a graph  $\mathcal{G}$  that encodes the geometric structure of  $q$ -space sampling points, and the DMRI signals in one voxel can be viewed as a function  $f$  defined on  $\mathcal{G}$ .

## 2.2 Graph Fourier Analysis

The graph Laplacian,  $L$ , is the key operator in graph Fourier analysis. Following [18], we define  $L = D - W$ , where  $D = \text{diag}\{d_1, d_2, \dots, d_N\}$  is a degree matrix with  $d_i = \sum_j w_{ij}$ . The graph Laplacian can be further normalized using

$$L = I - D^{-1/2} W D^{-1/2}, \quad (2)$$

where  $I$  is an identity matrix. We perform eigen decomposition for  $L$  to obtain  $L = U\Lambda U^\top$ , where  $U$  and  $\Lambda$  are matrices containing the eigenvectors and eigenvalues, respectively.

As discussed in [18],  $U$  can be viewed as the basis for graph Fourier transform (GFT). Therefore, we define the forward and inverse GFTs as  $\hat{f} = U^\top f$  and  $f = U\hat{f}$ , respectively, where  $\hat{f}$  is the Fourier coefficients. The convolution theorem states that convolution is equivalent to point-wise multiplication in the transform domain. This serves as the basis for spectral graph convolution. Given a convolution kernel function  $h$ , we have

$$h * f = U(U^\top h \odot U^\top f) = U(\hat{h} \odot \hat{f}) = U(\text{diag}(\hat{h})U^\top f), \quad (3)$$

where  $\odot$  represents a point-wise product and  $\text{diag}(\hat{h})$  is a diagonal matrix with diagonal elements specified by  $\hat{h}$ . However, this framework suffers from two limitations: (i) The eigen decomposition and forward/inverse GFT are computationally expensive; and (ii) The convolution is expected to be localized, but is not guaranteed to be so.

## 2.3 Fast and Localized Spectral Filtering

To address these two limitations, a fast and localized spectral filtering technique was proposed in [18]. Specifically, replacing  $\text{diag}(\hat{h})$  with another diagonal matrix,  $g_\theta(\Lambda)$ , parametrized by  $\theta$ , we then have

$$h * f = U(g_\theta(\Lambda)U^\top f) = g_\theta(U\Lambda U^\top)f = g_\theta(L)f. \quad (4)$$

The filter is now a function of the graph Laplacian, avoiding eigen decomposition and forward/inverse GFT. Computational complexity is therefore significantly reduced.

Direct learning of  $\theta$  involves a complexity of  $\mathcal{O}(N)$  and does not guarantee localized filters. These problems can be resolved by using a polynomial filter defined as

$$g_{\theta}(L) = \sum_{k=0}^K \theta_k L^k, \quad (5)$$

where  $\theta = [\theta_0, \theta_1, \dots, \theta_K] \in \mathbb{R}^{K+1}$  is a vector of polynomial coefficients. This reduces the learning complexity to  $\mathcal{O}(K)$ . Based on Parseval's theorem [18], smoothness in the spectral domain corresponds to the localization in the spatial domain. More specifically, the spectral filter approximated by the  $K$ -th order polynomials of the Laplacian is exactly  $K$ -localized. Following [18], we utilize Chebyshev polynomials  $T_K(\cdot)$  to design the filter, i.e.,

$$g_{\theta}(L)f = \sum_{k=0}^K \theta_k T_K(\tilde{L})f, \quad (6)$$

where  $\tilde{L}$  is the scaled Laplacian, defined as  $\tilde{L} = 2L / \lambda_{\max} - I$  with  $\lambda_{\max}$  being the maximal eigenvalue of  $L$ . Chebyshev polynomials have a recurrence relation, i.e.,  $T_k(\lambda) = 2\lambda T_{k-1}(\lambda) - T_{k-2}(\lambda)$  with  $T_1(\lambda) = \lambda$  and  $T_0(\lambda) = 1$ . Finally, a feature map  $f^{(l)}$  at the  $l$ -th graph convolutional layer is given by

$$f^{(l)} = \xi \left( \sum_{c=1}^C g_{\theta_c}^{(l)}(L) f_c^{(l-1)} + b^{(l)} \right), \quad (7)$$

where  $\xi(\cdot)$  is a non-linear activation function,  $f_c^{(l-1)}$  is the  $c$ -th channel feature map at the  $(l-1)$ -th layer,  $\theta_c^{(l)}$  is the corresponding learning parameters, and  $b^{(l)}$  is the bias.

## 2.4 Network Architecture

An overview of our network architecture is shown in Fig. 2. The input is sparsely sampled  $q$ -space data and the output is a vector of microstructural estimates. The input data is first fed to a graph convolutional layer followed by a leaky ReLU (LReLU) activation function. This is followed by two residual blocks, each with a graph coarsening layer. Each residual block consists of two graph convolutional layers, a LReLU activation function, and a residual skip connection to improve training [26]. We utilize the method described in [18] for graph coarsening to increase the receptive field, similar to the pooling operation in conventional CNNs for 2D/3D images [27]. After the second graph coarsening, a final graph convolution layer is employed to integrate the feature maps into a single map. The features from the map are fed into two fully-connected (FC) layers to predict the microstructure indices. The number of nodes in the first FC layer is identical to the number of elements in the input to the layer. The number of nodes in the second FC layer is determined by the number of microstructure indices that need to be estimated. As commonly done in regression tasks, we train the model using  $\ell_2$  loss:

$$\mathcal{L} = \frac{1}{N} \sum_{i=1}^N |M_i - \widehat{M}_i|, \quad (8)$$

where  $M_i$  is the  $i$ -th ground truth microstructural index,  $\widehat{M}_i$  is the corresponding estimate, and  $N$  is the number of microstructural indices.

### 3 Experiments

#### 3.1 Dataset

Our dataset consisted of 13 subjects randomly selected from the Baby Connectome Project (BCP) [16,17]. We utilized 5 of them for training and the rest for testing. All data were acquired using a Siemens 3T Magnetom Prisma MR scanner with the following imaging protocol:  $140 \times 105$  imaging matrix,  $1.5 \times 1.5 \times 1.5$  mm<sup>3</sup> resolution, TE = 88 ms, TR = 2,365 ms,  $b = 500, 1000, 1500, 2000, 2500, 3000$  s/mm<sup>2</sup>, and a total of 144 non-collinear gradient directions. All enrolled subjects had written informed consent provided by parents/guardians. The experimental protocols were approved by the Institutional Review Board of the University of North Carolina (UNC) School of Medicine.

#### 3.2 Implementation Details

We trained our network to predict NODDI [28] indices, including intra-cellular volume fraction (ICVF), isotropic volume fraction (ISOVF), and orientation dispersion index (ODI). To construct the training data, we computed NODDI indices from the complete DMRI data (144 DWIs) of all training subjects using AMICO [29] as prediction targets. The DMRI data was subsampled uniformly in  $q$ -space with factors 2 (72 DWIs), 3 (48 DWIs), and 4 (36 DWIs). Finally, we randomly selected 20,000 voxels from the brain region of each training subject to form our training dataset with a total of 100,000 samples. The testing dataset was created in a similar way, but using the DMRI data of testing subjects. Note that the network was trained separately for the different subsampling rates.

The proposed network was implemented using TensorFlow 1.2 [30]. In all experiments, we trained the network using the ADAM optimizer [31] with an initial learning rate of 0.01 and an exponential decay rate of 0.95. Other hyperparameters were set as follows: (1) The polynomial order  $K$  was set to 10. (2) The number of feature maps for each residual block was set to 8. (3) We set  $\sigma_a = \sqrt{1 - \cos^2(30^\circ)} \approx 0.5$ , where the angular degree  $30^\circ$  was determined by grid search from  $10^\circ$  to  $50^\circ$ . (4) Since our data is shell-sampled, we set  $\sigma_b$  to a small value, 0.1. An early stopping strategy was adopted to prevent over-fitting. The network was trained using a computer equipped with an NVIDIA GeForce GTX 1080 Ti GPU with 11 GB RAM. We utilized AMICO and MLP as our comparison baselines. Multilayer perceptron (MLP) was implemented based on [9] with the same network architecture and hyper-parameters.

#### 3.3 Results

We first performed quantitative evaluations using the peak signal-to-noise ratio (PSNR) as the metric. The results, shown in Fig. 3, indicate that GCNN outperforms two baseline

methods in all cases. Particularly, the overall PSNR values for all indices, shown in the right of Fig. 3, indicate that GCNN improves estimation accuracy for all three subsampling rates. In contrast, AMICO fails to provide satisfactory results when the subsampling rate is larger than 2. MLP gives poor performance, in comparison with the other two methods, when the subsampling rate is 2.

The ICVF maps, shown in Fig. 4, further confirm our conclusions based on Fig. 3. For all subsampling factors, GCNN gives high-quality ICVF maps that are close to the gold standard. For better visualization, we computed the ICVF error maps for different methods and subsampling factors. The results, shown in Fig. 4, indicate that GCNN reduces estimation errors.

Finally, we compared the computation times of different methods. All the methods were tested using a computer equipped with a four-core 2.9 GHz Intel Core i7 CPU. For fair comparison, MLP and GCNN were set to operate in CPU mode. The results, shown in Table 1, indicate that both MLP and GCNN reduce the computation time significantly. Specifically, the two DL methods are at least 70 times faster than AMICO, facilitating microstructural estimation in large-scale studies.

## 4 Conclusion and Future Work

In this work, we have proposed a framework for estimating tissue microstructure using graph CNNs. Our method makes full use of information from angular neighbors in  $q$ -space, and thus improves estimation accuracy. The experiments on BCP data indicate that our method yields microstructure index maps with improved quality.

In the future, we will evaluate our network performance thoroughly by performing cross-validation on some well-known DMRI datasets, e.g., Human Connectome Project [32]. We will also investigate the influence of hyper-parameters, including the polynomial order and the number of filters. Finally, we will utilize our network to predict microstructure indices given by other diffusion models, such as DKI [4].

## Acknowledgments

This work was supported in part by NIH grants (NS093842, EB006733, MH104324, and MH110274) and the efforts of the UNC/UMN Baby Connectome Project Consortium.

## References

1. Hagmann P, Jonasson L, Maeder P, Thiran JP, Wedeen VJ, Meuli R: Understanding diffusion MR imaging techniques: from scalar diffusion-weighted imaging to diffusion tensor imaging and beyond. *Radiographics* 26, S205–S223 (2006) [PubMed: 17050517]
2. Jones DK: *Diffusion MRI*. Oxford University Press, Oxford (2010)
3. Johansen-Berg H, Behrens TE: *Diffusion MRI: from quantitative measurement to in vivo neuroanatomy*. Academic Press (2013)
4. Jensen JH, Helpert JA, Ramani A, Lu H, Kaczynski K: Diffusional kurtosis imaging: the quantification of non-gaussian water diffusion by means of magnetic resonance imaging. *Magnetic Resonance Med.* 53(6), 1432–1440 (2005)

5. Zhang H, Schneider T, Wheeler-Kingshott CA, Alexander DC: NODDI: practical in vivo neurite orientation dispersion and density imaging of the human brain. *Neuroimage* 61(4), 1000–1016 (2012) [PubMed: 22484410]
6. Kaden E, Kruggel F, Alexander DC: Quantitative mapping of the per-axon diffusion coefficients in brain white matter. *Magnetic Resonance Med.* 75(4), 1752–1763 (2016)
7. Huynh KM, et al.: Characterizing non-gaussian diffusion in heterogeneously oriented tissue microenvironments. In: Shen D, et al. (eds.) MICCAI 2019. LNCS, vol. 11766, pp. 556–563. Springer, Cham (2019). 10.1007/978-3-030-32248-9\_62
8. Huynh KM, et al.: Probing tissue microarchitecture of the baby brain via spherical mean spectrum imaging. *IEEE Trans. Med. Imag* (2020)
9. Golkov V, et al.: Q-space deep learning: twelve-fold shorter and model-free diffusion MRI scans. *IEEE Trans. Med. Imag* 35(5), 1344–1351 (2016)
10. Ye C: Tissue microstructure estimation using a deep network inspired by a dictionary-based framework. *Med. Image Anal* 42, 288–299 (2017) [PubMed: 28910696]
11. Li Z, et al.: Fast and robust diffusion kurtosis parametric mapping using a three-dimensional convolutional neural network. *IEEE Access* 7, 71398–71411 (2019)
12. Ye C, Li X, Chen J: A deep network for tissue microstructure estimation using modified LSTM units. *Med. Image Anal* 55, 49–64 (2019) [PubMed: 31022640]
13. Gibbons EK, et al.: Simultaneous NODDI and GFA parameter map generation from subsampled q-space imaging using deep learning. *Magnetic Resonance Med.* 81(4), 2399–2411 (2019)
14. Ye C, et al.: Super-resolved  $q$ -space deep learning. In: Shen D, et al. (eds.) MICCAI 2019. LNCS, vol. 11766, pp. 582–589. Springer, Cham (2019). 10.1007/978-3-030-32248-9\_65
15. Ye C, Li Y, Zeng X: An improved deep network for tissue microstructure estimation with uncertainty quantification. *Med. Image Anal* 61, 101650 (2020) [PubMed: 32007700]
16. Fallik D: The human connectome project turns to mapping brain development, from birth through early childhood. *Neurol. Today* 16(19), 7–8 (2016)
17. Howell BR, et al.: The UNC/UMN baby connectome project (BCP): an overview of the study design and protocol development. *NeuroImage* 185, 891–905 (2019) [PubMed: 29578031]
18. Defferrard M, Bresson X, Vandergheynst P: Convolutional neural networks on graphs with fast localized spectral filtering. In: *Advances in Neural Information Processing Systems*, pp. 3844–3852 (2016)
19. Kim J, Hong Y, Chen G, Lin W, Yap P-T, Shen D: Graph-based deep learning for prediction of longitudinal infant diffusion MRI Data. In: Bonet-Carne E, Grussu F, Ning L, Sepehrband F, Tax CMW (eds.) MICCAI 2019. MV, pp. 133–141. Springer, Cham (2019). 10.1007/978-3-030-05831-9\_11
20. Hong Y, Chen G, Yap P-T, Shen D: Multifold acceleration of diffusion MRI via deep learning reconstruction from slice-undersampled data. In: Chung ACS, Gee JC, Yushkevich PA, Bao S (eds.) IPMI 2019. LNCS, vol. 11492, pp. 530–541. Springer, Cham (2019). 10.1007/978-3-030-20351-1\_41
21. Hong Y, Kim J, Chen G, Lin W, Yap PT, Shen D: Longitudinal prediction of infant diffusion MRI data via graph convolutional adversarial networks. *IEEE Transactions on Medical Imaging* (2019)
22. Hong Y, Chen G, Yap PT, Shen D: Reconstructing high-quality diffusion MRI data from orthogonal slice-undersampled data using graph convolutional neural networks. In: *International Conference on Medical Image Computing and Computer-Assisted Intervention*, pp. 529–537 (2019)
23. Chen G, Dong B, Zhang Y, Lin W, Shen D, Yap PT: Denoising of infant diffusion MRI data via graph framelet matching in  $x$ - $q$  space. *IEEE Transactions on Medical Imaging* (2019)
24. Chen G, Wu Y, Shen D, Yap PT: Noise reduction in diffusion MRI using non-local self-similar information in joint  $x$ - $q$  space. *Med. Image Anal* 53, 79–94 (2019) [PubMed: 30703580]
25. Chen G, Dong B, Zhang Y, Lin W, Shen D, Yap PT: XQ-SR: joint  $x$ - $q$  space super-resolution with application to infant diffusion MRI. *Med. Image Anal* 57, 44–55 (2019) [PubMed: 31279215]
26. He K, Zhang X, Ren S, Sun J: Deep residual learning for image recognition. In: *Proceedings of the IEEE Conference on Computer Vision and Pattern Recognition*, pp. 770–778 (2016)



27. LeCun Y, Bottou L, Bengio Y, Haffner P, et al.: Gradient-based learning applied to document recognition. *Proc. IEEE* 86(11), 2278–2324 (1998)
28. Sone D: Neurite orientation and dispersion density imaging: clinical utility, efficacy, and role in therapy. *Reports Med. Imag* 12, 17 (2019)
29. Daducci A, Canales-Rodríguez EJ, Zhang H, Dyrby TB, Alexander DC, Thiran JP: Accelerated microstructure imaging via convex optimization (AMICO) from diffusion MRI data. *NeuroImage* 105, 32–44 (2015) [PubMed: 25462697]
30. Abadi M, et al.: Tensorflow: a system for large-scale machine learning. In: 12th USENIX Symposium on Operating Systems Design and Implementation (OSDI 16). pp. 265–283 (2016)
31. Kingma DP, Ba J: Adam: a method for stochastic optimization. *arXiv preprint arXiv:1412.6980* (2014)
32. Van Essen DC, et al.: The WU-Minn human connectome project: an overview. *NeuroImage*, 80 62–79 (2013) [PubMed: 23684880]



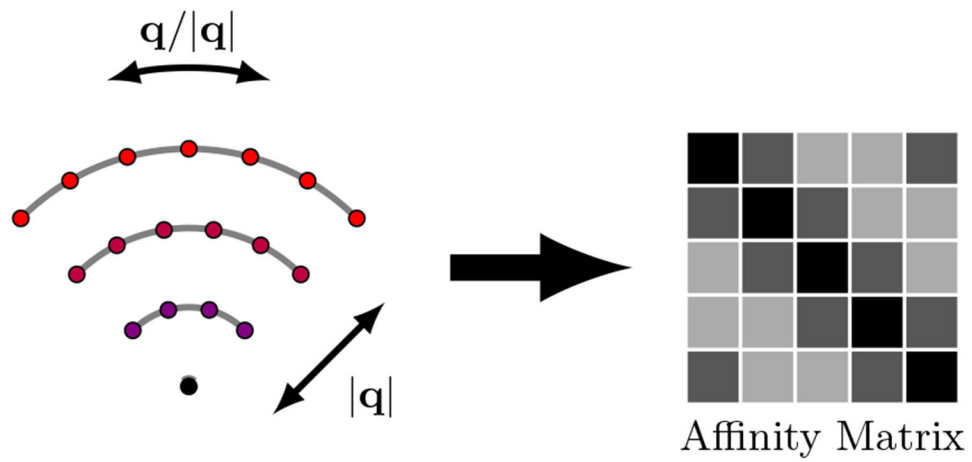


**Fig. 1.**  
Graph representation of  $q$ -space.

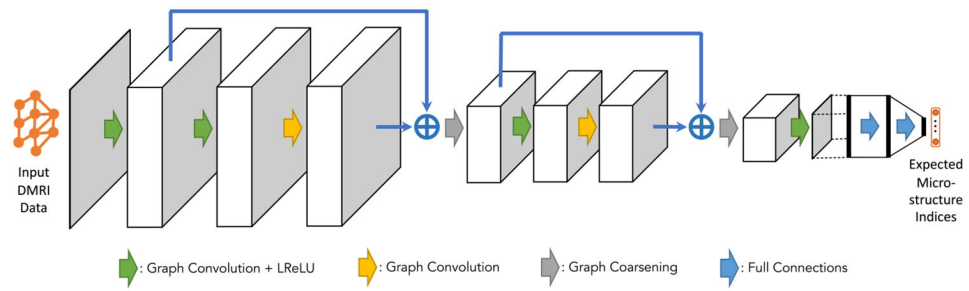


**Fig. 2.**  
An overview of the proposed GCNN.

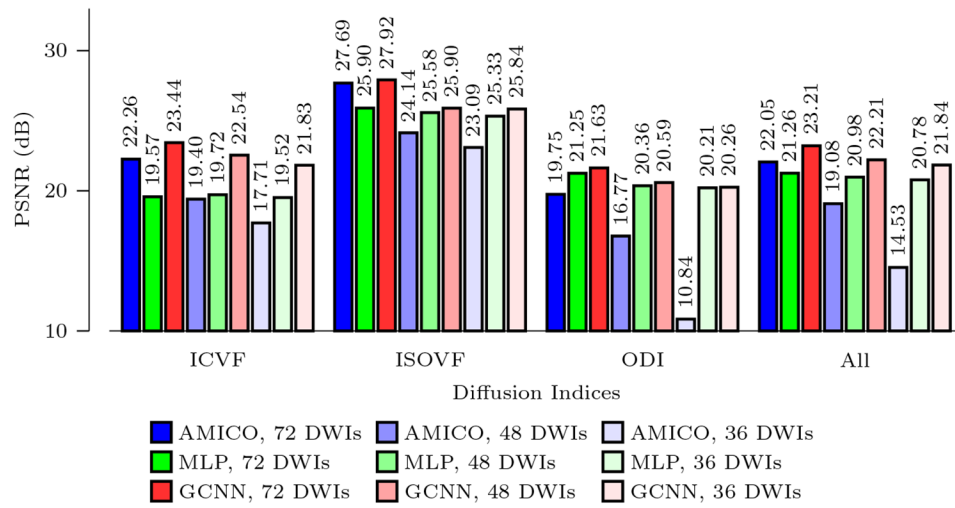


**Fig. 3.**  
Average PSNR values computed across the eight testing subjects.

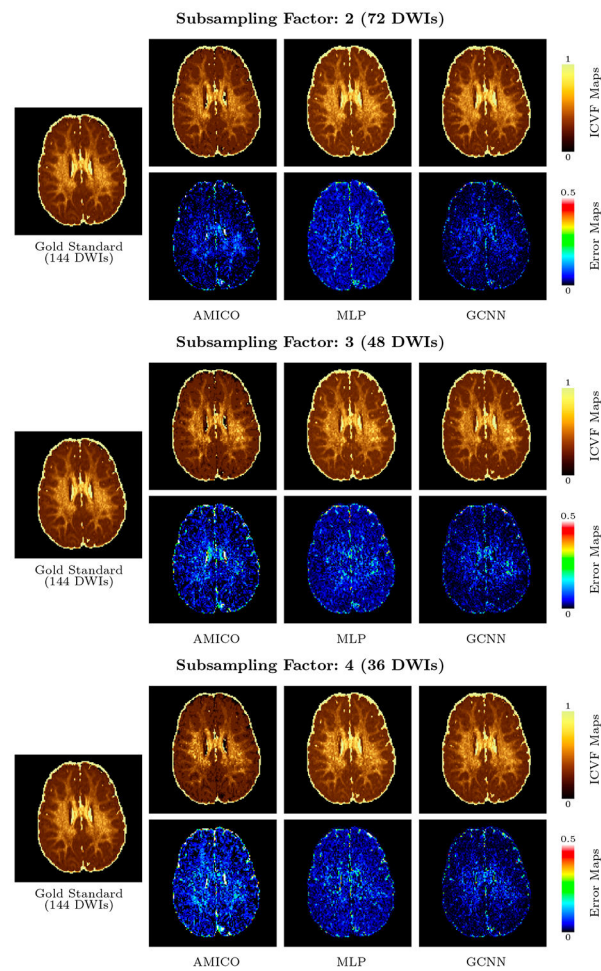


**Fig. 4.**  
Visual comparison of ICVF maps and associated error maps.

**Table 1.**

Computation time based on totally 395,515 voxels in the brain region of a randomly selected testing subject.

	AMICO	MLP	GCNN
Time (s)	2,252.3	19.2	32.1

Author Manuscript

Author Manuscript

Author Manuscript

Author Manuscript